Investigation of the flow phenomena in high-pressure water jet nozzles

Oleg Urazmetov [a,*], Marcel Cadet [b], Roman Teutsch [b], Sergiy Antonyuk [a]

[a] Institute of Particle Process Engineering, Technische Universität Kaiserslautern, Gottlieb-Daimler-Str. 44, 67663 Kaiserslautern, Germany

[b] Institute for Mechanical and Automotive Design, Technische Universität Kaiserslautern, Gottlieb-Daimler-Str. 42, 67663 Kaiserslautern, Germany

ARTICLE INFO

ABSTRACT

High-pressure water jets are often used as a tool for cleaning, cutting or for modification of the surface morphology. The nozzle design has a considerable influence on cavitation and wear effects as well as on the nature of the exiting jets. Different applications are affected by different flow regimes, such as cavitation or hydraulic-flip, which depend on the radius of the nozzle edge.

In this work, the turbulent two-phase flow within two different nozzle types is analyzed using Computational Fluid Dynamics. The focus was to establish a relationship between the geometry of these nozzles and the flow phenomena as well as between wall shear stress and the wear, which leads to the change of the water jet shape and reduces the lifetime of high-pressure nozzles. The performed variation of the nozzle edge from sharp to round showed a significant influence on the maximum wall shear stress and cavitation. Additionally, the inner surface of used nozzles was investigated with Scanning Electron Microscope. Numerous marks of erosion were found at the nozzle edge. For the validation, the volumetric flow rate through the nozzles was measured at different inlet pressures and compared with the simulation results, which showed a good agreement.

© 2020 Institution of Chemical Engineers. Published by Elsevier B.V. All rights reserved.

1. Introduction

High-pressure water jet (HPWJ) nozzles with circular orifices are available for different applications, such as cleaning, cutting, deburring and modification of surface morphology. In the chemical industry, the pressure of HPWJ nozzles for cleaning go up to approximately 50 MPa. Whereas in classical mechanical engineering HPWJ nozzles are mostly used to transfer forces onto metallic or concrete materials. Therefore, correspondingly higher operating pressures in the range from 100 MPa to 600 MPa are required (Powell, 2017). To cut metallic or any other material effectively, abrasives are mixed to form an abrasive water jet (Hashish, 1988).

Depending on the geometry of the HPWJ nozzle, different flow forms occur within the nozzle. For cutting processes, HPWJ nozzles with a sharp inlet edge are used, which generate the so-called *hydraulic-flip* (Tafreshi and Pourdeyhimi, 2004). This flow state inside the nozzle allows a coherent and stable water jet with low turbulence. High-pressure nozzles for cleaning applications have a cone-capillary geometry and generate a turbulent water jet. It is known from the literature that cone-capillary nozzles have a higher discharge coefficient and therefore deliver a higher energy per unit time (Begenir et al., 2004). However, the cone-capillary nozzles form a partially atomized water jet and have a shorter break-up length when compared to capillary nozzles (Anantharamaiah et al., 2006).

In many works, flow behavior in different shaped nozzles was studied both numerically and experimentally. The pioneer work of Wolfgang von Ohnesorge in 1936 (Ohnesorge, 1936) described for the first time the droplet formation and atomization of liquid jets. His findings provided flow regimes of liquid jets at different Reynolds and Weber numbers. Later, inspired by the development of more efficient diesel engines, the atomization of diesel fuel was extensively researched (Bergwerk, 1959). More detailed investigations of instabilities in liquid jets were made possible by high-speed photography (Hoyt and Taylor, 1977). A methodical investigation of the jet breakup pro-

---

Nomenclature

A_0	Reference area (m^2)
α	Volume fraction (–)
C_d	Nozzle discharge (–)
μ	Viscosity (Pa s)
σ	Surface tension coefficient (N m^{-1})
ρ	Density (kg m^{-3})
ρ_0	Reference density (kg m^{-3})
K_0	Bulk modulus (Pa)
$\dot{m}$	Mass flow (kg s^{-1})
m	Mass (kg)
n	Density exponent (–)
n_B	Bubble number density (–)
p	Pressure (Pa)
p_0	Reference pressure (Pa)
$\dot{q}$	Volume flow rate (m^3 s^{-1})
R	Bubble radius (m)
Re	Reynolds number (–)
t	Time (s)
k_l	Turbulence kinetic energy (J/kg)
U_{Bern}	Jet velocity at constant density (m s^{-1})
U_{th}	Theoretical jet velocity (m s^{-1})

Abbreviations

CFD	Computational Fluid Dynamics
HPWJ	High-pressure water jet
STEP	Standard for the exchange of product model data
STL	Stereolithography
μCT	Micro-computed tomography
SEM	Scanning electron microscopy
EDX	Energy dispersive X-ray spectroscopy

cess can be found in (Kuo, 1996). The modelling of the primary breakup of high-speed jets remains challenging to this day and one of the first approaches was made by (Yi and Reitz, 2004).

In more recent years, Ghassemieh et al. (2006) investigated experimentally the flow of small water jets with pressures up to 12 MPa. Their findings showed that a sharp inlet edge in capillary nozzles is responsible for flow detachment. They also reported that wear of nozzles depends on the nozzle material, the volume flow rate and the water hardness. Due to wear, the efficiency of the water jet is reduced and the nozzle must be replaced. Small solid particles can cause chipping of the orifice in ceramic-based nozzles (Susuzlu et al., 2004). Anantharamaiah et al. (2006) performed a numerical study on the degradation of pure water jet nozzles with pressures up to 20 MPa. Their findings provided evidence that the degradation of steel nozzles takes place because of stress-induced corrosion. They also examined cone-capillary and capillary nozzles and gave an overview of the operating conditions. Another type of wear is erosion by cavitation, which mainly depends on the design of the nozzle edge radius, (Simpson and Ranade, 2018). Abrasive wear due to solid particles can also occur with poor water quality in steel nozzles (Wright et al., 2003).

The rounding of the inlet edge of a nozzle has a great influence on the shape of the liquid jet. The ratio of the nozzle edge radius to the orifice diameter is commonly referred as r/d. A simple expression for predicting of the inlet roundness for capillary nozzles was published by Anantharamaiah et al. (2007). Experimental investigations of free water jets (Gong et al., 2016; Hoyt and Taylor, 1977) have shown the immense influence of nozzle flow on atomization at higher Reynolds numbers. Another important factor for nozzles is the ratio of nozzle length to nozzle diameter, commonly referred to as l/d. The ratio of l/d together with the Reynolds number, influences the jet turbulence, jet

breakup length and the discharge coefficient (Lefebvre and McDonell, 2017). Cavitation phenomena commonly occur due to the presence of a sharp edge, which causes a deflection of the flow. With smaller l/d ratios, the vapor cavitation bubbles can directly reach the nozzle outlet. A larger l/d ratio has the opposite effect (Zandi et al., 2015).

In addition, cavitation affects the water jet break-up. Sou et al. (2007) showed the effect of cavitation on atomization in two-dimensional like nozzles and defined different regimes of cavitation. It turned out that super cavitation lead to a spray forming at the nozzle outlet, whereas a further increase of cavitation causes the hydraulic-flip regime.

Cavitation is a phenomenon which is used in various processes, see for example (Bałdyga et al., 2009; Duerkop et al., 2018; Niazi et al., 2014). However, the cavitation can lead to increased wear of a component as an undesirable side effect (Haosheng et al., 2007).

Due to high pressures, the experimental study of the flow inside the nozzle is difficult or not possible. Numerical simulations can make an important contribution to understanding the flow process within the high-pressure nozzles (Annoni et al., 2014). In a study performed in (Zandi et al., 2015) cavitation was numerically investigated in a nozzle for diesel atomization. This study showed that with the increasing cavitation the discharge coefficient decreases. The reason for this is the constriction of the cross-section of the orifice by the vapor phase.

In this paper, a detailed numerical investigation of the flow in two nozzle types is presented. For the first nozzle type, a capillary nozzle with a sharp inlet edge, the hydraulic-flip was simulated at different pressure values. In the second nozzle type, a cone-capillary nozzle, the cavitation phenomena, which can lead to severe wear, were numerically investigated at different pressures and radii of the inlet edge. A further aim of the performed investigation was the quantification of the wall shear stresses in the two nozzle types that cause or contribute to wear, especially in steel nozzles (Wright et al., 2003). Additionally, the wear patterns on both nozzles were examined and compared with the simulation results. For both nozzle types, volumetric flow rate measurements and water jet visualizations were carried out and compared with the simulations.

2. Materials and methods

2.1. Modeling of the two-phase flow

The model of a two-phase flow used in this work is based on the mixture approach (Manninen et al., 1996), where each of the two fluids may penetrate each other. For both phases, only one continuity and one momentum equation are solved. Therefore, no interaction between the two phases, such as surface tension, is taken into account by the simulation. The fluid properties are calculated on a mass-weighted average basis. The continuity equation is given by:

$$\frac{\partial}{\partial t}\left(\rho_m\right) + \nabla \cdot \left(\rho_m \vec{v}_m\right) = 0, \tag{1}$$

where $\vec{v}_m = \sum_{k=1}^{n} \frac{\alpha_k \rho_k \vec{v}_k}{\rho_m}$ is the mass-averaged velocity and $\rho_m = \sum_{k=1}^{n} \alpha_k \rho_k$ is the mixture density with α_k as the volume fraction of the phase k, which was defined as water and air for the capillary nozzle and water and vapor for the cone-capillary nozzle.

The equation of momentum of the mixture is given by:

$$\frac{\partial}{\partial t}\left(\rho_m \vec{v}_m\right) + \nabla \cdot \left(\rho_m \vec{v}_m \vec{v}_m\right) = -\nabla p$$
$$+ \nabla \cdot \left[\mu_m \left(\nabla \vec{v}_m + \nabla \vec{v}_m^T\right)\right], \tag{2}$$

with the viscosity of the mixture $\mu_m = \sum_{k=1}^{n} \alpha_k \mu_k$.

For the cavitation modeling the Schnerr-Sauer model was used (Sauer et al., 2000), which describes the mass transfer from liquid to vapor by the vapor transport equation:

$$\frac{\partial}{\partial t}\left(\alpha \rho_v\right) + \nabla \cdot \left(\alpha \rho_v \vec{V}_v\right) = R_e - R_c, \tag{3}$$

where ρ_v is the vapor density and $\vec{V}_v$ is the vapor phase velocity. On the right-hand side, R_e and R_c are the source terms, which connect the growth and the collapse of the vapor bubbles, respectively.

The Rayleigh–Plesset equation is used to describe the bubble growth depending on the local pressure (Sauer et al., 2000):

$$R_B \frac{d^2 R_B}{dt^2} + \frac{3}{2}\left(\frac{dR_B}{dt}\right)^2 = \frac{p_v - p}{\rho_l} - \frac{2\sigma}{\rho_l R_B} - 4\frac{\mu_l}{\rho_l R_B}\frac{dR_B}{dt}, \tag{4}$$

where R_B describes the bubble radius, p_v is the partial pressure of vapor (index v, vapor), p is the local pressure, ρ_l is the density of liquid (index l, liquid), and σ is the surface tension. By neglecting the second-order terms and the surface tension force, Eq. (4) can be simplified to:

$$\frac{dR_B}{dt} = \sqrt{\frac{2\left(p_v - p\right)}{3\rho_l}}. \tag{5}$$

The cavitation flow is modeled as being isothermal with no latent heat of vaporization. The growth and collapse flow rates of bubbles are modeled as follows:

$$R_e = F_{vap}\frac{\rho_v \rho_l}{\rho}\alpha\left(1 - \alpha\right)\frac{3}{R_B}\sqrt{\frac{2\left(p_v - p\right)}{3\rho_l}},\; p_v > p,$$

$$R_c = F_{cond}\frac{\rho_v \rho_l}{\rho}\alpha\left(1 - \alpha\right)\frac{3}{R_B}\sqrt{\frac{2\left(p - p_v\right)}{3\rho_l}},\; p_v < p, \tag{6}$$

where F_{vap} and F_{cond} are empirical coefficients, which were set to 1 and 0.2, respectively (Khaware et al., 2019). The mixture density is defined as $\rho = \alpha \rho_v + (1 - \alpha)\rho_l$, with α as the vapor volume fraction, which describes the volume fraction of spherical bubbles per volume of the computational cell:

$$\alpha = \frac{n_B \frac{4}{3}\pi R_B^3}{1 + n_B \frac{4}{3}\pi R_B^3}. \tag{7}$$

The following equation considers the influence of turbulence on vapor pressure:

$$p_v = p_{sat} + \frac{1}{2}T\rho_l k_l, \tag{8}$$

where p_{sat} is the saturation pressure of vapor, T is the turbulence coefficient which has a default value of 0.39, this value is reported originally by Singhal et al. (2002), and k_l is the turbulence kinetic energy. The bubble radius R_B is calculated as follows:

$$R_B = \left(\frac{\alpha}{1 - \alpha}\frac{3}{4\pi}\frac{1}{n_B}\right)^{\frac{1}{3}}. \tag{9}$$

The bubble number density n_B can be determined from experiments (Brennen, 1995).

2.2. Theoretical velocity of the high-pressure water jet

Since water becomes compressible at sufficiently high pressure, the velocity calculation will be affected by the compressibility. The following three equations are used to calculate the velocity of the jet with water as a compressible liquid (Susuzlu et al., 2004). The equation of state for the density is given by:

$$\rho_l = \rho_0\left(1 + \frac{p}{nK_0}\right)^n, \tag{10}$$

where ρ_0 is the standard water density (25 °C, 1 bar), n is the density exponent and K_0 is the reference bulk modulus, which describes the compressibility of the water and depends on temperature and pressure (Susuzlu et al., 2004). From Eq. (10) and Bernoulli's equation:

$$U_{bern} = \sqrt{\frac{2p}{\rho}}, \tag{11}$$

the theoretical jet velocity U_{th} can be found as:

$$U_{th} = \sqrt{\frac{2nK_0}{\rho_0\left(1 - n\right)}\left[\left(1 + \frac{p}{nK_0}\right)^{1-n} - 1\right]}. \tag{12}$$

At $p = 325\,\text{MPa}$ and a constant density of 998.2 kg/m³, Eq. (11) gives the velocity $U_{bern.} = 806.95$ m/s. With compressible density, the density increases up to 1155 kg/m³ at $p = 325\,\text{MPa}$, $n = 7.15$ and $K_0 = 2.2\,\text{GPa}$ (at 25 °C, value rises with pressure) (Walker et al., 2008). Due to the compressibility of the water, the speed of the water jet changes slightly, resulting in $U_{th} = 778.23$ m/s see Eq. (12). The difference is around 3.5%.

Another important value for nozzle flow is the nozzle discharge coefficient C_d, which can be calculated from the real volume flow rate $\dot{q}$ as:

$$C_d = \frac{\dot{q}}{A_0 U_{th}}, \tag{13}$$

where A_0 is the cross section area of the nozzle outlet.

2.3. Geometry, numerical mesh and parameters

The studied capillary nozzle had a nominal diameter of 80 μm and a sapphire orifice insert. This nozzle is available from various manufacturers under the name: sapphire nozzle type 18. The investigated cone-capillary nozzle was purchased from WOMA® (Form 21LL) and has a nominal diameter of 500 μm. The geometries of the nozzles were obtained from μCT scans (Fig. 1), which were performed with a *Werth Tomo Scope*® *HV Compact* tomograph. For the 500 μm nozzle the resolution of the scan was sufficient and it turned out that the orifice had a slightly smaller diameter of 489 μm. The data from μCT scan were used for the mesh generation, but in the further course of this paper, we still refer to this nozzle as 500 μm. For the 80 μm nozzle, the scan was insufficient to resolve the small orifice. Therefore, in the CFD simulation we assumed the diameter to be 80 μm as it was specified by the manufacturer. The STL geometry files obtained from the μCT scans were transferred to STEP 3D geometry files using a reverse engineering process. Based on the geometry, the computational mesh was created. For the first nozzle type, the whole flow domain was used for the simulation. For the second nozzle type, only the inter-
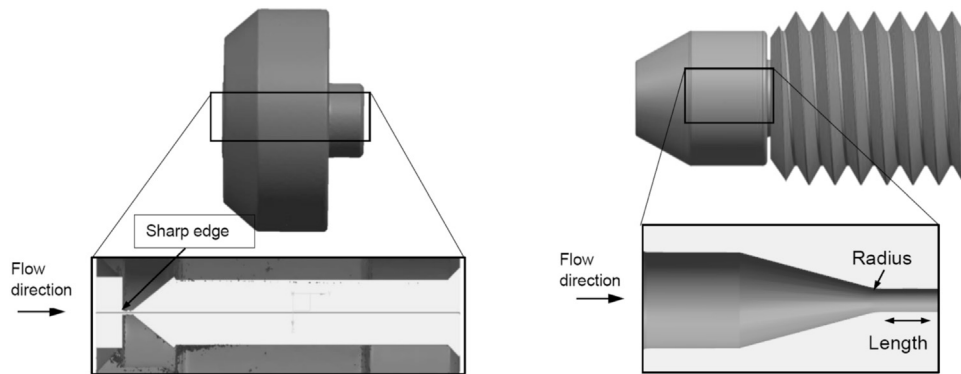
Fig. 1 – Reconstructed geometries of studied nozzles obtained from μCT scans: (left) capillary nozzle with sharp edge (r = 0 mm) and 80 μm orifice diameter (sapphire nozzle of the type 18), (right) cone-capillary nozzle with 500 μm orifice diameter and edge radius of approximately 1 mm (WOMA® Form 21LL).

Table 1 – Mesh independence analysis for the conical nozzle at 750 bar.			
	Coarse	Medium	Fine
Number of cells	1,176,902	1,270,103	1,370,978
Dimensionless wall distance y^+	7.7	0.47	0.28
Mass flowrate / kg/s	0.06906	0.06935	0.06938
Max. velocity / m/s	384.62	384.62	384.62

nal geometry was simulated to investigate the effects on wall shear stress and cavitation.

Square grid elements were used for the simulations and areas of interest were refined using the method of hanging nodes. Mesh independence analysis was carried out exemplarily with the conical nozzle at a pressure of 750 bar. The original mesh was locally refined several times to achieve a y^+ value less than unity. The results are summarized in Table 1. The largest deviations in the mass flowrate were found between the coarse and medium mesh. Further refinement from medium to fine did not result in a large deviation. Therefore, a y^+ value <0.5 was set for both nozzle types in all simulations of this study.

Boundary conditions and mesh for the two nozzles are depicted in Fig. 2. For the 80 μm capillary nozzle, the influence of the pressure on the nozzle discharge coefficient and on the maximum wall shear stress is studied. Three inlet pressures were simulated: 125 MPa, 200 MPa and 325 MPa. In all simulations of this nozzle, the nozzle edge radius and the length of the capillary were constant at 0.08 mm and 0.17 mm, respectively. This results in a ratio of nozzle edge radius to the orifice diameter of r/d = 0 and a nozzle length to nozzle orifice diameter of l/d = 2.125.

Whereas the 500 μm cone-capillary nozzle besides the inlet pressure variation, 75 MPa, 125 MPa and 200 MPa, three different nozzle edge radii were examined: r = 0 mm, r = 0.1 mm and r = 1 mm. The obtained effects on the flow behavior and cavitation are evaluated depending on the corresponding ratio between the edge radii to the nozzle orifice diameters: r/d = 0, r/d = 0.2 and r/d = 2, see Fig. 2b. The ratio of nozzle length to the nozzle orifice diameter results in l/d = 2.5. All cases were defined as 2D-axisymmetric.

All numerical simulations were performed with Ansys Fluent 19.0 applying a steady state approach. The kω-SST turbulence model has been selected, since it shows good predictions on adverse pressure gradients and separation of the flow. Additionally the viscous boundary layer can be resolved with a fine mesh (Menter, 1994). For the modeling of the cav-

itation, we assumed a constant "bubble number density" n_B of 10^{13} see Eq. (7) since many authors reported good results using this value (Li et al., 2010; Liu, 2013; Shi et al., 2019). With the turbulence coefficient of 0.39, local pressure fluctuations are taken into account in the cavitation model (Soriano Palao, 2009). For the numerical convergence, both the residuals and values of interest, such as mass flow imbalance, maximum flow velocity and maximum wall shear stress were monitored during the simulation.

2.4. Experimental setup

Volumetric flow rates through the two studied nozzles at different pressures were measured and photographs of the water jets were taken. The pumps UHDE HP19/45-S and 45M/P12-1502/P20 were used for the capillary nozzle and cone-capillary nozzle respectively. A Nikon d7200 CMOS camera with a Zeiss 50 mm, f/2 lens was utilized with a Nanolite 120 ns flash system. Photographs were taken in a completely dark room with a relatively slow shutter speed of 1/15 s. Therefore, only the light from the Nanolite flash exposed the sensor. The aperture was set to f/2, which provided good light intensity and a sufficient depth of field (Urazmetov et al., 2019).

In the case of the capillary nozzle, the water was collected in a container for the volumetric flow measurement and the time was measured. For the cone-capillary nozzle, which has a larger orifice, an ultrasonic flow meter was used.

The wear signs of the nozzles were examined with two different Scanning Electron Microscopes (SEM). With the capillary nozzle, the images were taken by a SEM Thermo Fisher Phenom 2G pro, while the Hitachi SU8000 was used with the cone-capillary nozzle.

3. Simulation results

3.1. Capillary nozzle

The velocity magnitude in the capillary nozzle at three simulated pressures is presented in Fig. 3. Depending on the inlet pressure (125 MPa, 200 MPa and 325 MPa), the obtained maximum flow velocities are 495 m/s, 622 m/s and 785 m/s, respectively.

Fig. 3b shows the velocity profiles inside the nozzle for the 125 MPa inlet pressure as the ratio of the flow velocity U to the theoretical velocity U_{th}, see Eq. (12), in three different locations as indicated in Fig. 3a. On the y-axis, the radial position Y in the nozzle is given in relation to the nozzle diameter d. The
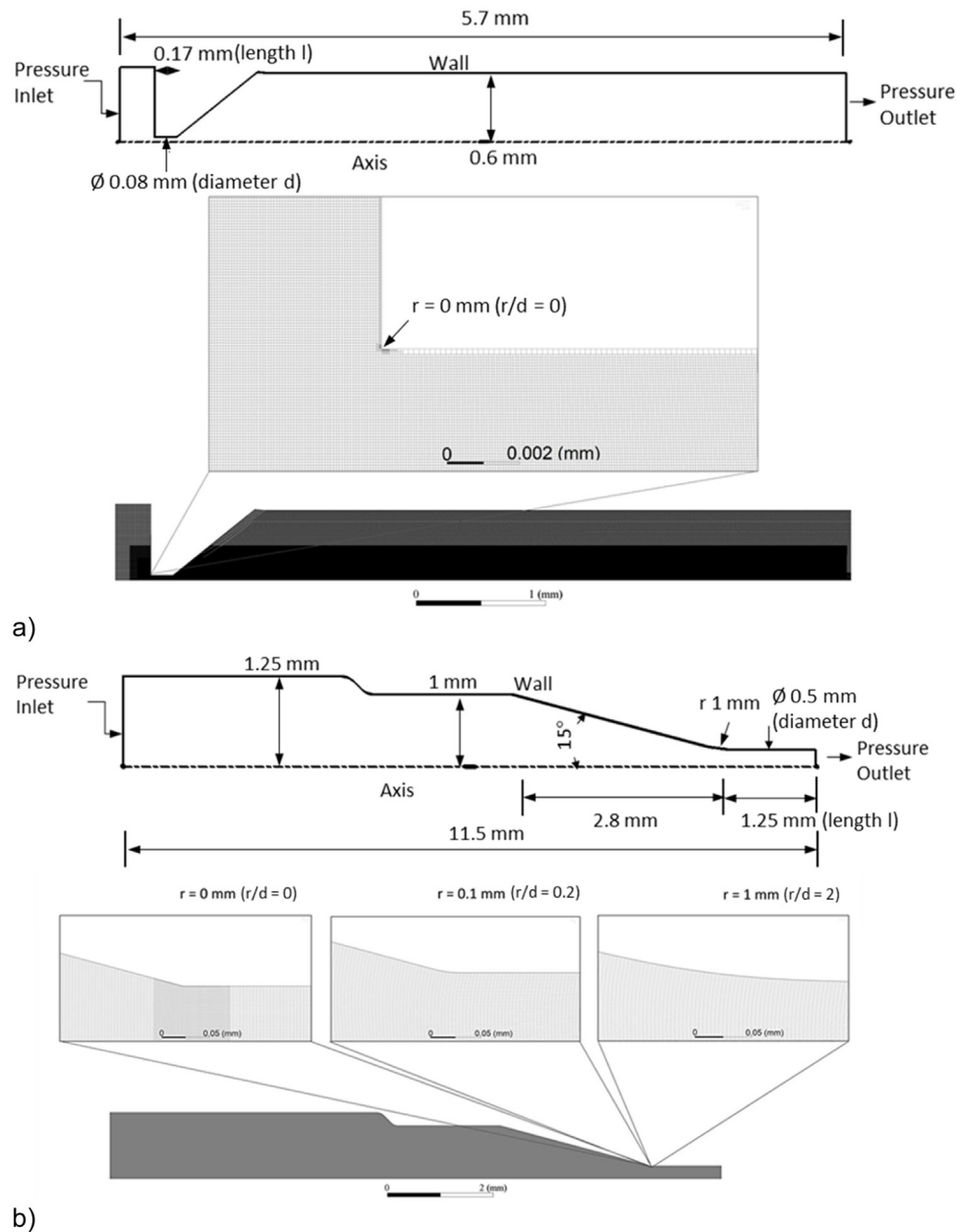
Fig. 2 – Boundary conditions, geometry and numerical mesh of the capillary nozzle (a) and the cone-capillary nozzle (b).

water flow at the inlet section of the nozzle has a high velocity gradient near the wall. At this location, the water jet is formed and interacts firstly with ambient air. The other two locations *nozzle mid* and *nozzle out* show that the airflow near to the wall moves in the opposite direction to the water jet.

The water jet is in the hydraulic-flip flow state for all three pressure values. The flow of the water is detached from the wall, which has been caused by cavitation inside the nozzle (Fig. 4a). When the vapor exits the nozzle, and it mixes with ambient air, thus replacing the vapor inside the nozzle, which prevents further cavitation. Near the wall of the orifice, the airflow can be observed, which is being pulled in by the low pressure of the water jet. This results in a stable water jet.

The airflow circulates inside the capillary of the nozzle (Fig. 4b). For this reason, in a zone between these two counter-streaming flows, at approximately Y/d = 0.45 the velocity is almost zero. Another interesting fact is that the air velocity reaches 140 m/s, i.e. about 30 % of water jet velocity. However, since the compressibility of air is being neglected, these findings must be taken with caution. Part of the airflow does not

enter the capillary of the nozzle and mixes with the airflow surrounding the water jet (Fig. 4b right). If there are droplets in this area, they will be drawn in by the airflow into the water jet, which will lead to a disturbance of the water jet as was shown in the simulation of Annoni et al. (2014).

A higher inlet pressure leads to a higher flow velocity and thus to a higher Reynolds number. Fig. 4c shows the discharge coefficient obtained for the capillary nozzle. The discharge coefficient is slightly influenced by the Reynolds number. Increasing the Reynolds number by 1.7 times (from 36,000 to 62,000) increases the discharge coefficient less than by 2.5% (from 0.612 to 0.627), which is caused by the compressibility of water.

The simulation of the capillary nozzle reveals high wall shear stresses at the nozzle edge. In order to show the shear stress distribution in the most stressed area, the wall shear stress was plotted in Fig. 5a from the nozzle edge to about 2 μm into the nozzle interior. The position of 40 μm corresponds to the sharp edge on the nozzle, where the flow detaches from the wall. The wall shear stress decreases rapidly with
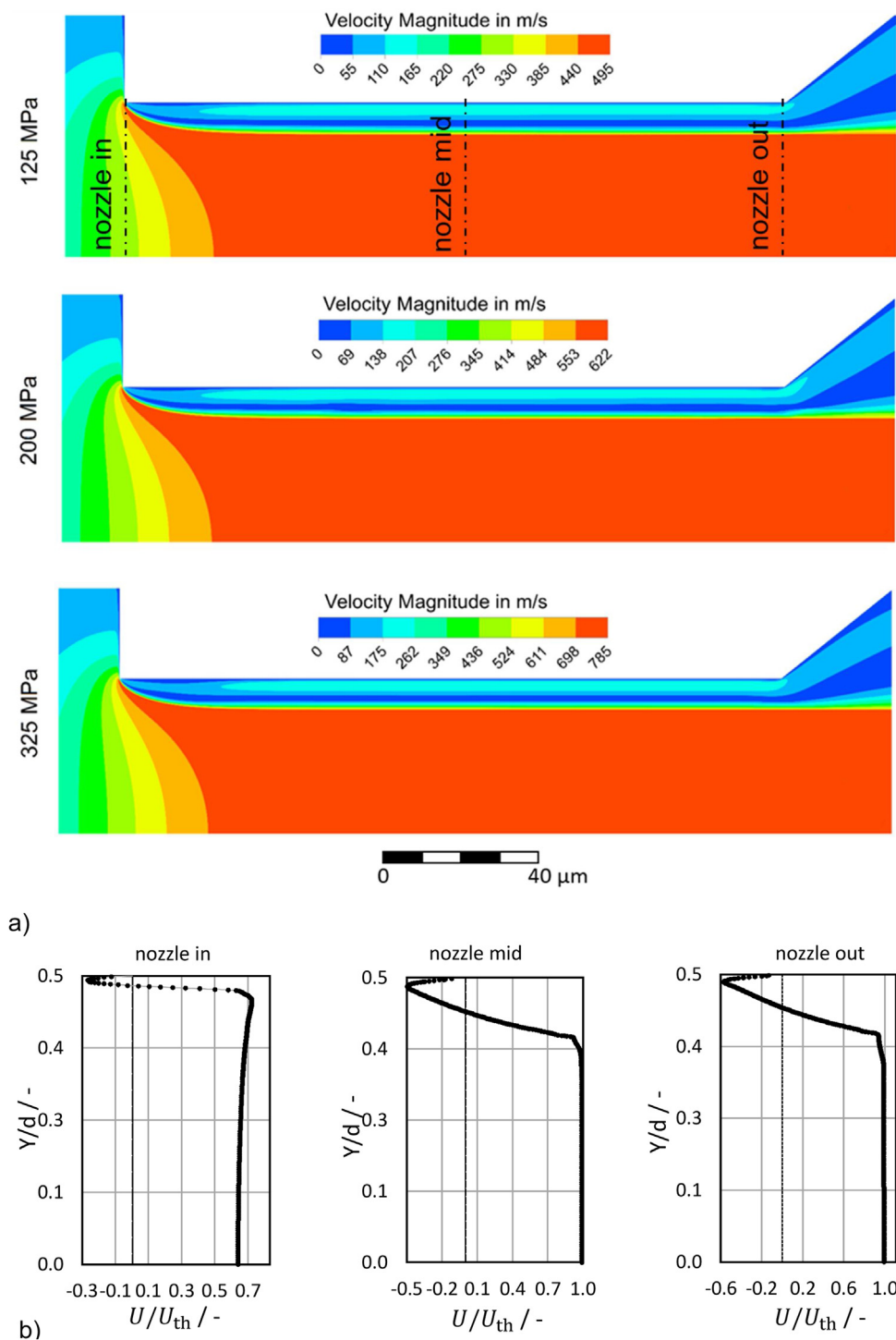
Fig. 3 – a) Velocity magnitude in the capillary nozzle at different pressures, b) velocity profiles at three locations of the capillary nozzle at 125 MPa.

increasing radial position from the nozzle edge. Although the absolute wall shear stress increases with increasing inlet pressure, the normalized values of the wall shear stress display a reversed effect, Fig. 5b. This can also be explained by the fact that the water is compressible, similar to the greater difference between the velocities at constant and variable density.

3.2. Cone-capillary nozzle

The flow velocity distribution inside the cone-capillary nozzle obtained by the simulation with the original geometry from µCT scans is shown in Fig. 6a. In this figure, three different nozzle edge radii are compared for a constant nozzle orifice

diameter. The flow was calculated at inlet pressures of 75 MPa, 125 MPa and 200 MPa. Contrary to the capillary nozzle, where the flow detaches from the wall, no flow separation in the cone-capillary nozzle occurs. At the rounded transition from conical to cylindrical orifice part of the nozzle, a very thin boundary layer can be observed which leads to the highest values of shear stress in this region of the nozzle. The width of the boundary layer increases in the direction of the nozzle outlet.

As expected, a higher inlet pressure leads to a higher flow velocity and the maximum values of 385 m/s, 495 m/s and 622 m/s are reached at 75 MPa, 125 MPa and 200 MPa, respectively. The nozzle with the ratio of radius to diameter of 2 shows
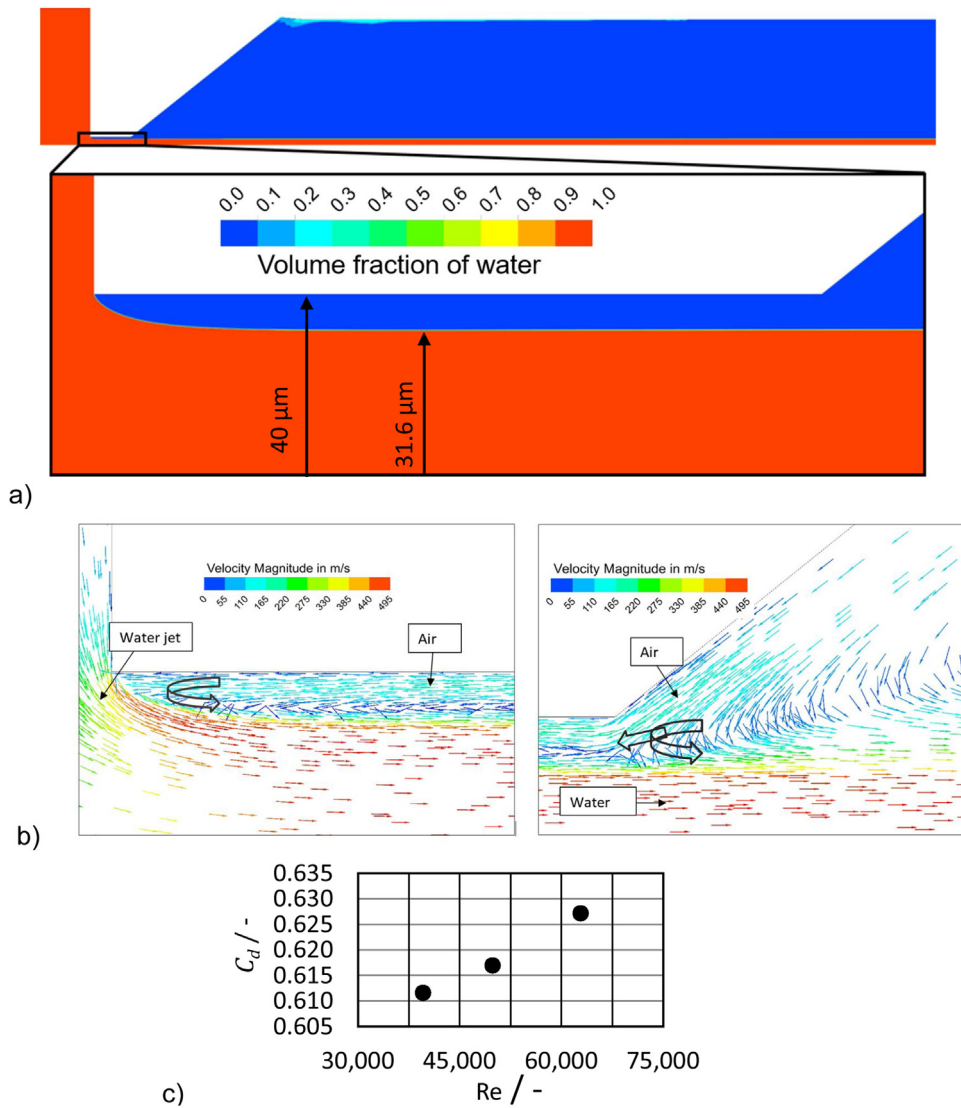
Fig. 4 – a) Hydraulic-flip flow condition and b) vectors of velocity in the capillary nozzle at 125 MPa, at *nozzle in* location (left) and at *nozzle out* location (right), c) discharge coefficient.
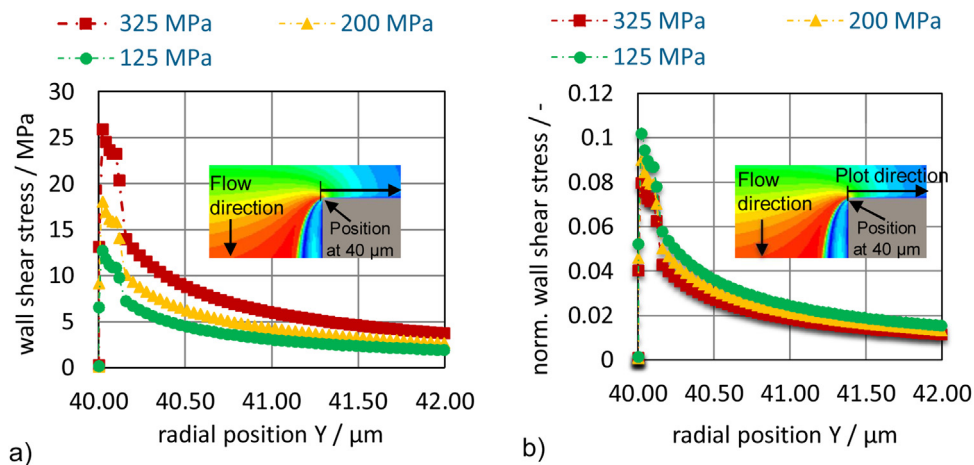

Fig. 5 – a) Wall shear stress at the inlet edge, b) normalized (wall shear stress divided by inlet pressure) wall shear stress obtained for the capillary nozzle.

a more uniform velocity profile. For nozzles with sharp edge and with the radius to diameter ratio of 0.2, a higher velocity gradient at the nozzle edge can be observed.

Fig. 6b compares the cavitation effects in the nozzles with the sharp edge (r/d = 0) and edge with the smaller radius (r/d

= 0.2). The water is accelerated due to the narrowing of the cross-section. When the nozzle edge is reached, the following scenarios can occur depending on the geometry. If the radius of the nozzle edge is large enough so that the water flow can follow the contour of the nozzle, no cavitation occurs. At a
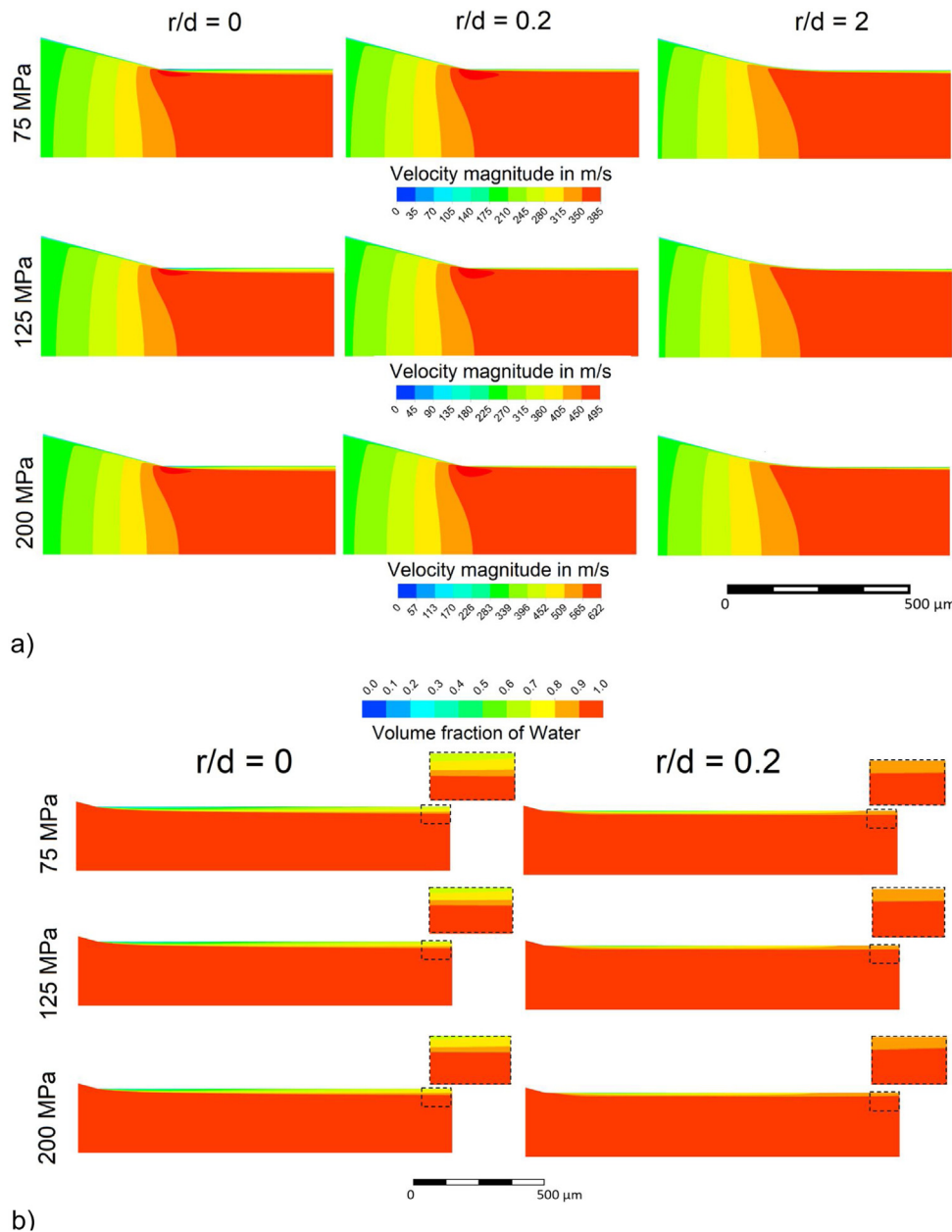
Fig. 6 – a) Velocity magnitude for three r/d ratios and b) cavitation at the sharp edge (r/d = 0) and the small radius (r/d = 0.2) in cone-capillary nozzle at three different pressures.

sharp edge or at a smaller radius, the flow cannot follow the contour of the nozzle and detaches from the wall, which leads to a backflow. As a result, a strong negative gauge pressure is created in the backflow area. If pressure falls below the vapor pressure, a phase transition takes place resulting in formation of vapor bubbles and cavitation. In areas with a higher pressure, the vapor bubbles collapse. The cavitation zone is very thin and the nozzle with r/d = 0 exhibits higher cavitation than the r/d = 0.2 nozzle. In the nozzle with sharp edge, r/d = 0, the vapor reaches the nozzle outlet, which can significantly influence the atomization of the water jet (Sou et al., 2007). For the r/d = 0.2 nozzle most of the vapor condenses before reaching the nozzle outlet. The r/d = 2 nozzle was not affected by cavitation in the simulation.

Fig. 7 shows the velocity profile at the nozzle outlet at different inlet pressures. It is evident that the velocity profiles are significantly influenced by cavitation. Interestingly, the nozzle r/d = 0.2 has a velocity profile with the smallest boundary layer, which can be explained by the condensation of the

vapor phase. The condensation disturbs the development of the velocity profile. The nozzle with the sharp edge produces a higher amount of vapor, which does not fully condense. Thus, a mixture of water and vapor exits the nozzle. As expected, the velocity profile for the r/d = 2 nozzle shows a small increasing velocity gradient with increasing pressure.

The predicted discharge coefficient at different operation parameters is presented in Fig. 8a and b. The discharge coefficient increases with the Reynolds number for all varied radii. This can be attributed to the reduction of the viscous sublayer and the compressibility of the water that subsequently leads to a higher discharge value.

Due to occurring cavitation, a contraction of the effective cross-section takes place. Therefore, the sharp edge at r/d = 0 leads to a lower discharge coefficient. For the same reason, the discharge coefficient at the smaller radius of r/d = 0.2 is in between. The influence of r/d ratios on the flow coefficient is depicted in Fig. 8b. The increase of r/d from 0 to 0.2
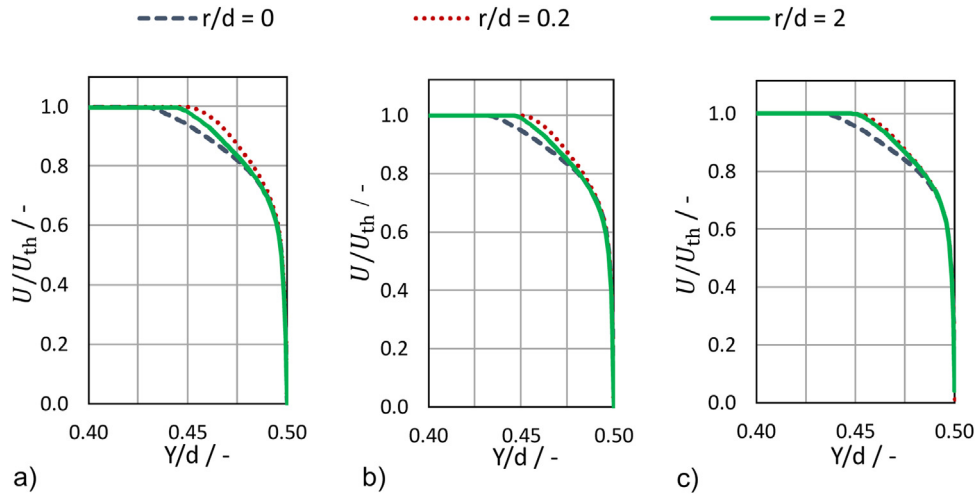
Fig. 7 – Influence of pressure on the velocity profile at the outlet of the cone-capillary nozzle for different ratios of radius to diameter r/d at: a) 75 MPa, b) 125 MPa, and c) 200 MPa.
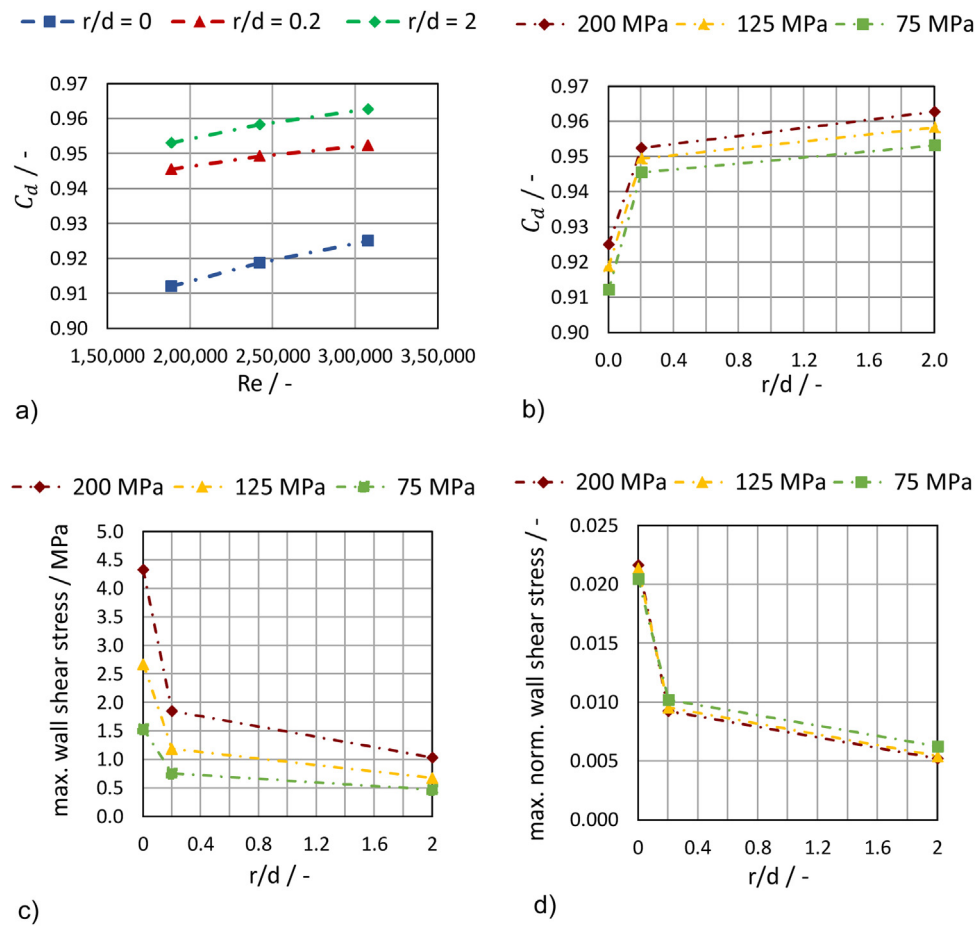

Fig. 8 – Influence of radius to diameter ratio r/d of cone-capillary nozzle on the discharge coefficient C_d at different Reynolds numbers (a) and pressures (b) as well as on the maximum (c) and normalized (d) wall shear stress at different pressures.

Table 2 – Volume flow rate for the capillary nozzle (Ø 80 μm) and cone-capillary nozzle (Ø 500 μm and r/d = 2).

Pressure	Capillary nozzle			Cone-capillary nozzle		
	Simulation flow rate in l/min	Experiment flow rate in l/min	Div. in %	Simulation flow rate in l/min	Experiment flow rate in l/min	Div. in %
75 MPa	–	–	–	4.1	4.0	−3.7
125 MPa	0.0919	0.1025	+10.5	5.3	5.5	+2.7
200 MPa	0.117	0.126	+7.6	6.7	6.9	+2
325 MPa	0.149	0.158	+6	–	–	–
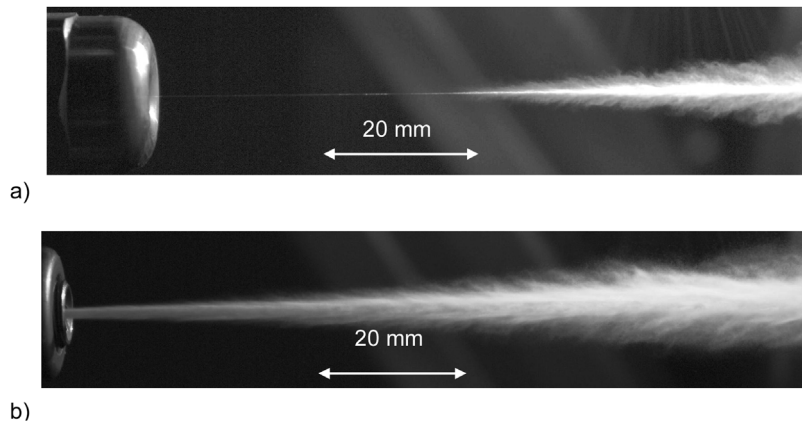
Fig. 9 – a) High-speed photograph of a water jet generated by the studied capillary nozzle with orifice diameter of 80 μm at 125 MPa. b) High-speed photograph of a water jet generated by the studied cone-capillary nozzle with the orifice diameter of 500 μm at 75 MPa, r/d = 2.

has a greater influence on the discharge coefficient than the increase from 0.2 to 2.

When calculating the maximum wall shear stress, a strong dependency on the nozzle radius was found, Fig. 8c. A drop in the maximum wall shear stress of about 50% was observed at the nozzle with the small radius, r/d = 0.2, compared to the nozzle with the sharp edge, r/d = 0. The sharp edge r/d = 0 leads to cavitation and to the highest calculated wall shear stress. As expected, the maximum wall shear stress also depends on the inlet pressure. The same behavior was determined for the capillary nozzle. The maximum calculated wall shear stress is located near the nozzle edge. Comparing the results of the wall shear stress for both investigated nozzle types, one can see that the cone-capillary nozzle with a sharp edge achieves a significantly lower normalized wall shear stress than the capillary nozzle (compare Fig. 5b to Fig. 8d). The convergent shape of the nozzle reduces the maximum wall shear stress at the nozzle edge.

4. Experimental results

4.1. Volume flow rate measurements

The volumetric flow rate through the capillary nozzle was measured gravimetrically. The results are given in Table 2. The deviation of the measurements from the simulations amounted to 6–8% for the inlet pressure of 200 MPa and 325 MPa, and to approximately 10% for the pressure of 125 MPa. These deviations are caused by the following factors: pressure build-up when opening the valve and pressure fluctuations during operation. The higher volumetric flow rate of the cone-capillary nozzle was measured with an ultrasonic flow meter on the feed pipe of the pump. The results showed a good agreement with the simulation.

4.2. High-speed photography

High-speed images were taken to evaluate the shapes of water jets, Fig. 9. At first, the water jet from the capillary nozzle is evaluated. The water jet has a laminar, glass-like structure at the nozzle outlet, Fig. 9a. The photo demonstrates the initiation of the break-up at a length of approx. 40 mm. The reason for this is the formation of the hydraulic-flip, which was obtained with the simulation for this nozzle type in Section 3.1. The hydraulic-flip

reduces the disturbances, which can occur due to wall friction or cavitation. After reaching its break-up length, the water jet atomizes very strongly due to the aerodynamic effects.

The water jet produced by the cone-capillary nozzle is shown in Fig. 9b. Compared to the water jet from the capillary nozzle, the cone-capillary nozzle shows a much more turbulent water jet at the nozzle exit. It has a milky surface which is caused by light scattering from ruffles on the surface (Lefebvre and McDonell, 2017). This turbulent behavior is due to the non-detached flow of water inside the cone-capillary nozzle, as was obtained by the simulation in Section 3.2.

4.3. SEM imaging

Scanning Electron Microscope (SEM) images were used to evaluate the signs of wear for both nozzles. First, an unused and a used capillary nozzle were investigated with SEM (Fig. 10a). On an unused capillary nozzle, the nearly ideal round shape of the orifice was observed. The used capillary nozzle has white areas on the nozzle edge, which indicate first marks of abrasive erosion caused by particles impacts. In this region the highest wall shear stress values were predicted with the simulation. Due to the strong acceleration of the flow as showed in the simulation, solid particles can chip the surface. In addition, deposits of particles can be seen, near the nozzle edge. In particular, strong limescale deposits within the capillary were noticed.

To investigate erosion phenomena occurring inside the cone-capillary nozzle, the nozzle was operated at a pressure of approximately 95 MPa for a period of three hours and was mill-cut along the plane of symmetry. The largest and more frequent appearances of erosion were found on the rounded edge of the nozzle, see SEM images in Fig. 10b. The damage therefore appears at the location where the highest wall shear stresses occur. It is conceivable that the damage was caused by cavitation. Each nozzle is subject to manufacturing tolerances and a slightly higher roughness could lead to flow separation and cavitation in that area. With the help of an EDX (Energy Dispersive X-ray spectroscopy) analysis, the area around the eroded zone was examined more closely (Fig. 10c). A cavity was formed in which increased values of calcium were determined.
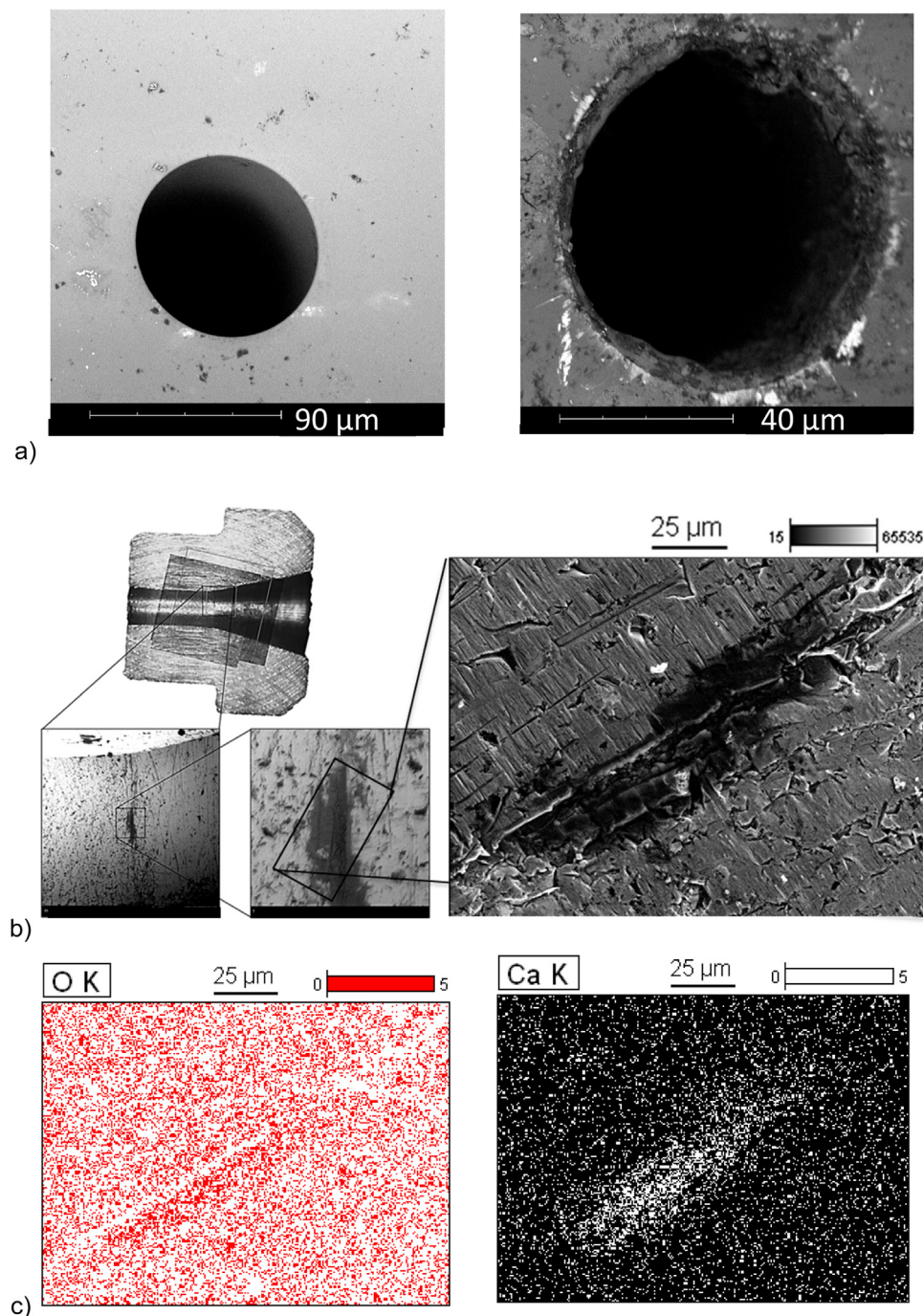
Fig. 10 – a) SEM images of an *unused* (left) and *used* (right) 80 μm capillary nozzle (inlet of the orifice), **b)** SEM images of a used cone-capillary nozzle, first marks of erosion (dark region) at the nozzle radius, **c)** EDX analysis of a used cone-capillary nozzle.

5. Conclusions

In this work, two different high-pressure water jet nozzles were investigated. The first type of nozzle has a sharp nozzle edge and a capillary orifice and is used mainly in cutting applications whereas the second type has a rounded nozzle edge and cone-capillary geometry and is used mainly for surface processing. For these applications, different water jets regimes are preferred, which mainly depend on the flow phenomena inside the nozzle.

For a detailed study of the nozzles, CFD with multiphase and cavitation models were applied. A real geometry of experimentally investigated nozzles was determined by μCT imaging and high-resolution numerical meshes were derived.

From simulations, detailed velocity profiles and wall shear stress distributions inside both nozzle types were obtained. The increasing of the inlet pressure led to an increase of the maximum wall stress for both nozzle types. In addition, when comparing the normalized wall shear stresses, significantly higher values were calculated for the capillary nozzle than for the cone-capillary nozzle. The maximum wall shear stress was located at the nozzle edge for both nozzle types. Based on SEM images, wear patterns in the nozzle edge area were observed. A connection of wall shear stress and signs of wear was established. Mechanisms such as erosion corrosion or abrasive erosion, caused by solid particles, lead to erosion of the nozzle edge. The latter can be assisted by the wall shear stress as our investigations suggest. Although stress induced

wear patterns were visible, the capillary nozzle operated in the hydraulic-flip regime. As long as the nozzle edge remains geometrically intact, the flow will separate and hydraulic-flip will occur. For the capillary nozzle made of sapphire, a sharp edge remains a good design choice for achieving the hydraulic-flip.

The geometry variation performed on the cone-capillary nozzle demonstrated that a higher curvature of the edge results in a lower wall shear stress and can significantly reduce cavitation that can lead to a higher wear resistance of a nozzle. Cavitation also has an influence on the velocity profile at the nozzle outlet, since the vapor phase interferes with the development of the velocity profile. The vapor phase narrows the cross-section of the nozzle, which affects the discharge coefficient. With increasing cavitation, the discharge coefficient decreases. With steel cone-capillary nozzles, cavitation can greatly reduce the service life of the nozzle and should therefore be avoided.

Declaration of interests

The authors declare that they have no known competing financial interests or personal relationships that could have appeared to influence the work reported in this paper.

Acknowledgements

References

Anantharamaiah, N., Tafreshi, H.V., Pourdeyhimi, B., 2006. A study on flow through hydroentangling nozzles and their degradation. Chem. Eng. Sci. 61 (14), 4582–4594, http://dx.doi.org/10.1016/j.ces.2006.01.038.

Anantharamaiah, N., Tafreshi, H.V., Pourdeyhimi, B., 2007. A simple expression for predicting the inlet roundness of micro-nozzles. J. Micromech. Microeng. 17 (5), N31–N39, http://dx.doi.org/10.1088/0960-1317/17/5/N01.

Annoni, M., Arleo, F., Malmassari, C., 2014. CFD aided design and experimental validation of an innovative air assisted pure water jet cutting system. J. Mater. Process. Technol. 214 (8), 1647–1657, http://dx.doi.org/10.1016/j.jmatprotec.2014.01.020.

Bałdyga, J., Makowski, Ł., Orciuch, W., Sauter, C., Schuchmann, H.P., 2009. Agglomerate dispersion in cavitating flows. Chem. Eng. Res. Des. 87 (4), 474–484, http://dx.doi.org/10.1016/j.cherd.2008.12.015.

Begenir, A., Vahedi Tafreshi, H., Pourdeyhimi, B., 2004. Effect of nozzle geometry on hydroentangling water jets; experimental observations. Text. Res. J. 74 (2), 178–184.

Bergwerk, W., 1959. Flow pattern in diesel nozzle spray holes. Arch. Proc. Inst. Mech. Eng. 173 (1), 655–660, http://dx.doi.org/10.1243/PIME_PROC_1959_173_054_02.

Brennen, C.E., 1995. Cavitation and Bubble Dynamics. Oxford University Press, New York, xv, 282.

Duerkop, M., Berger, E., Dürauer, A., Jungbauer, A., 2018. Influence of cavitation and high shear stress on HSA aggregation behavior. Eng. Life Sci. 18 (3), 169–178, http://dx.doi.org/10.1002/elsc.201700079.

Ghassemieh, E., Versteeg, H.K., Acar, M., 2006. The effect of nozzle geometry on the flow characteristics of small water jets. Proc. Inst. Mech. Eng. C J. Mech. Eng. Sci. 220 (12), 1739–1753, http://dx.doi.org/10.1243/0954406JMES430.

Gong, Chen, Yang, Minguan, Kang, Can, Wang, Yuli, 2016. Experimental study of jet surface structures and the influence of nozzle configuration. Fluid Dyn. Res.

Haosheng, C., Yongjian, L., Darong, C., Jiadao, W., 2007. Experimental and numerical investigations on development of cavitation erosion pits on solid surface. Tribol. Lett. 26 (2), 153–159, http://dx.doi.org/10.1007/s11249-006-9188-3.

Hashish, M., 1988. Visualization of the abrasive-waterjet cutting process. Exp. Mech. 28 (2), 159–169, http://dx.doi.org/10.1007/BF02317567.

Hoyt, J.W., Taylor, J.J., 1977. Waves on water jets. J. Fluid Mech. 83 (01), 119, http://dx.doi.org/10.1017/S0022112077001074.

Khaware, A., Gupta, V.K., Srikanth, K., Azhar, M., 2019. Numerical simulation of cavitating flows using overset mesh. In: The 4th World Congress on Momentum, Heat and Mass Transfer, 10.04.2019–12.04.2019. Avestia Publishing.

Kuo, K.K., 1996. Recent Advances in Spray Combustion: Spray Atomization and Drop Burning Phenomena. American Institute of Aeronautics and Astronautics, Washington DC, 520 pp.

Lefebvre, McDonell, 2017. Atomization and sprays. In: Combustion: An International Series, 2nd ed.

Li, D.-q., Grekula, M., Lindell, P., 2010. Towards numerical prediction of unsteady sheet cavitation on hydrofoils. J Hydrodyn 22 (S1), 699–704, http://dx.doi.org/10.1016/S1001-6058(10)60024-8.

Liu, H.-l., 2013. Application of modified κ-ω model to predicting cavitating flow in centrifugal pump. Water Sci. Eng. 6 (3), 331–339.

Manninen, M., Taivassalo, V., Kallio, S., 1996. On the Mixture Model for Multiphase Flow. Technical Research Centre of Finland, Espoo, 67 pp.

Menter, F.R., 1994. Two-equation eddy-viscosity turbulence models for engineering applications. AIAA Journal 32 (8), 1598–1605 https://doi.org/10.2514/3.12149.

Niazi, S., Hashemabadi, S.H., Razi, M.M., 2014. CFD simulation of acoustic cavitation in a crude oil upgrading sonoreactor and prediction of collapse temperature and pressure of a cavitation bubble. Chem. Eng. Res. Des. 92 (1), 166–173, http://dx.doi.org/10.1016/j.cherd.2013.07.002.

Ohnesorge, Wv., 1936. Die Bildung von Tropfen an Düsen und die Auflösung flüssiger Strahlen: Vorträge der Hauptversammlung in Dresden. Zeitschrift für angewandte Mathematik und Mechanik, 355–358 (Band 16, Heft 6).

Powell, M., 2017. Optimization of UHP waterjet cutting heads, the orifice. In: American WJTA Conference and Expo August 19–21, 2007, Houston, Texas.

Sauer, J., Winkler, G., Schnerr, G.H., 2000. Cavitation and condensation—common aspects of physical modeling and numerical approach. Chem. Eng. Technol. 23 (8), 663–666, http://dx.doi.org/10.1002/1521-4125(200008)23:8<663:AID-CEAT663>3.0.CO;2-H.

Shi, H., Li, M., Nikrityuk, P., Liu, Q., 2019. Experimental and numerical study of cavitation flows in venturi tubes: from CFD to an empirical model. Chem. Eng. Sci. 207, 672–687, http://dx.doi.org/10.1016/j.ces.2019.07.004.

Simpson, A., Ranade, V.V., 2018. Modelling of hydrodynamic cavitation with orifice: influence of different orifice designs. Chem. Eng. Res. Des. 136, 698–711, http://dx.doi.org/10.1016/j.cherd.2018.06.014.

Singhal, A.K., Athavale, M.M., Li, H., Jiang, Y., 2002. Mathematical basis and validation of the full cavitation model. J. Fluids Eng. 124 (3), 617–624, http://dx.doi.org/10.1115/1.1486223.

Soriano Palao, J.O., 2009. Modellierung des Einflusses der Düsenströmung auf den Zerfall von Dieselstrahlen – Dissertation. Universitäts- Und Landesbibliothek Sachsen-Anhalt; Martin-Luther Universität Halle-Wittenberg.

Sou, A., Hosokawa, S., Tomiyama, A., 2007. Effects of cavitation in a nozzle on liquid jet atomization. Int. J. Heat Mass Transf. 50 (17–18), 3575–3582, http://dx.doi.org/10.1016/j.ijheatmasstransfer.2006.12.033.

Susuzlu, T., Hoogstrate, A.M., Karpuschewski, B., 2004. Initial research on the ultra-high pressure waterjet up to 700 MPa. J. Mater. Process. Technol. 149 (1–3), 30–36, http://dx.doi.org/10.1016/j.jmatprotec.2003.11.044.

Tafreshi, Vahedi, Pourdeyhimi, B., 2004. Nonwovens Cooperative Research Center, North Carolina State University, Raleigh, NC, Cavitation and Hydraulic Flip. Fluent News spring 2004., pp. 38.

Urazmetov, O., Cadet, M., Teutsch, R., Schindler, C., Antonyuk, S., 2019. Experimental and numerical study of a high-pressure waterjet: ILASS-Europe 2019. In: 29th Conference on Liquid Atomization and Spray Systems, Paris, France.

Walker, J., Halliday, D., Resnick, R., 2008. Fundamentals of Physics, 8th ed. Wiley, Hoboken, NJ, 1 v. (various pagings).

Wright, D., Wolgamott, J., Zink, G., 2003. Waterjet Nozzle Material Types. StoneAge, Inc. Durango, Colorado, U.S.A. Houston, Texas, WJTA American Waterjet Conference.

Yi, Y., Reitz, R.D., 2004. Modeling the primary breakup of high-speed jets. Atomiz Spr 14 (1), 53–80, http://dx.doi.org/10.1615/AtomizSpr.v14.i1.40.

Zandi, A., Sohrabi, S., Shams, M., 2015. Influence of nozzle geometry and injection conditions on the cavitation flow inside a diesel injector. Int. J. Automot. Eng. 5 (1), 939–954.